IEEE Access
Multidisciplinary | Rapid Review | Open Access Journal

Received August 10, 2020, accepted August 14, 2020, date of publication August 18, 2020, date of current version August 28, 2020.

Digital Object Identifier 10.1109/ACCESS.2020.3017536

Complementary Split-Ring Resonator (CSRR)-Loaded Sensor Array to Detect Multiple Cracks: Shapes, Sizes, and Positions on Metallic Surface

AHMED SALIM, (Student Member, IEEE), AQEEL HUSSAIN NAQVI, (Student Member, IEEE), ANH DUC PHAM, (Student Member, IEEE), AND SUNGJOON LIM, (Member, IEEE)

School of Electrical and Electronics Engineering, Chung-Ang University, Seoul 06974, South Korea

Corresponding author: Sungjoon Lim (sungjoon@cau.ac.kr)

This work was supported by the National Research Foundation of Korea (NRF) funded by the Korean Government (MOE) under Grant 2017R1A2B3003856 and (MSIT) Grant 2018R1A4A1023826.

ABSTRACT Single-resonance-based radio frequency (RF) resonators cannot detect multiple cracks simultaneously nor localize the position of a crack. To address these drawbacks, we propose a complementary split-ring resonator (CSRR)-loaded array. In this array, there are four channels and each channel consists of three CSRRs, forming a 4 × 3 sensing array that is developed in the ground plane of a microstrip line using a low-cost FR4 substrate. A voltage-controlled oscillator (VCO) generates three discrete frequencies: 1.88 GHz, 2.60 GHz, and 3.61 GHz to each channel, which is sequentially selected using a single-pole four-throw (SP4T) switch. The transmitted RF signals are converted into the DC voltage levels and are interpreted by a microcontroller. Aluminum sheets with cracks embedded in the surface are used to demonstrate the detection of cracks of various shapes, sizes and locations/orientations (horizontal, diagonal, and vertical) with simulations and measurements. The detection of the minimum detectable crack ($W_c \times L_c \times D_c = 1$ mm × 10 mm × 0.1 mm) is experimentally verified. Full-length longer cracks ($L_c = 100$ mm) are also detected using our proposed detection system with the SP4T switch in addition to our proposed algorithm that scans the CSRRs of each selected channel.

INDEX TERMS Crack sensor, multiple cracks, RF sensor, crack detector, resonance.

I. INTRODUCTION

Structural health monitoring (SHM) is a diverse field that includes the continuous monitoring of structures and their constituting parts, non-destructive diagnoses of anomaly states, and the prognosis of future implications for preventive measures. The aging of materials, environmental effects, construction errors, stress that exceeds the load-carrying capacity, and natural disasters can induce fatigue, cracks in the materials, or even a collapse of the structure without any obvious signs.

Radiofrequency (RF) technology includes sensing devices that have gained much attention in research owing to attractive features such as low cost, simpler fabrication, and smaller sizes compared with non-RF crack sensors. A variety of RF resonators have been proposed to detect cracks on metallic surfaces. For instance, in [1] and [2], a patch antenna utilizing transverse magnetic $(TM)_{01}$ and TM_{10} modes is presented in which crack propagation (width, length, and direction) was characterized in [1]. However, cracks symmetrically occurring around the center axis of the patch antenna were indistinguishable [2]. In [3], an X-band frequency selective surface consisting of several cross-shaped unit cells realized on a polyimide film is proposed to detect metallic cracks in large-area structures.

Complementary split-ring resonators (CSRR) are one of the most popular topologies of metamaterials. In [4], a CSRR is loaded on the ground plane of the substrate integrated

The associate editor coordinating the review of this manuscript and approving it for publication was Wen-Sheng Zhao.

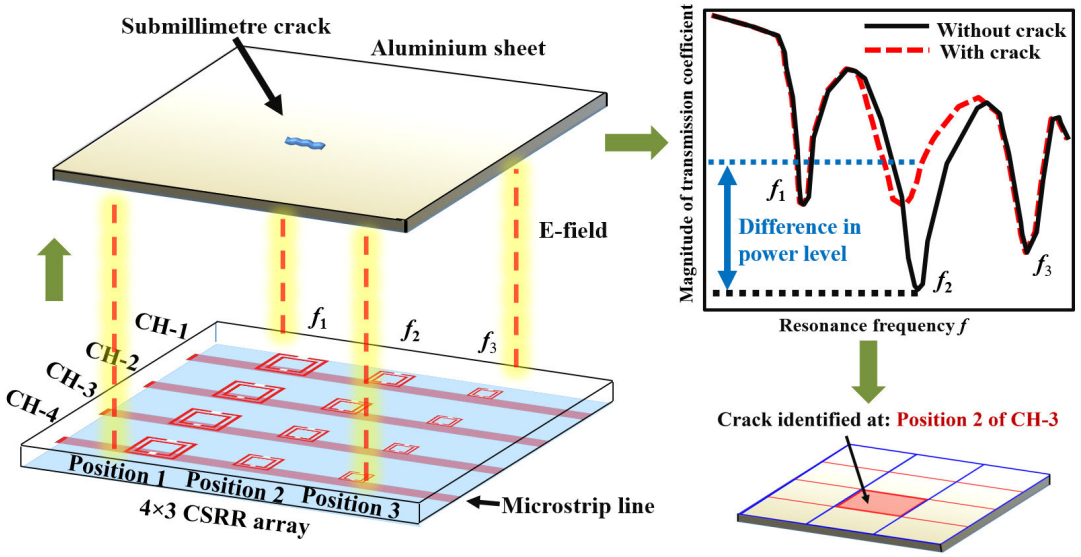

FIGURE 1. Sensing mechanism of the 4 × 3 CSRR-loaded sensor array employed in our proposed crack detection system.

waveguide (SIW) structure to detect a 1-mm-wide crack in a 5-mm thick aluminum (Al) sheet. A lower sensitivity owing to impedance mismatch and lower Q-factor is observed when surface roughness is increased. In [5] a CSRR is patterned on the ground plane of a microstrip line to detect cracks in an aluminum sheet. To enhance the sensitivity and resolution, the study suggests to fill a crack with a liquid dielectric material; therefore, a crack (0.2 mm wide and 2 mm deep) was filled with silicon oil (dielectric constant = 2.7) and, using a lumped element inductor (with an inductance of 20 nH) at the gap opening of the CSRR, miniaturization of the CSRR was also achieved. In existing literature (discussed in the last section), most of the RF crack sensors detect only a single crack and are incapable to identify the position of a crack. We address these serious limitations of single resonance based RF crack sensors.

We propose a CSRR-loaded array to detect multiple cracks. CSRRs consist of two electrically coupled slots etched on the ground plane of a microstrip line. The normal component of the electric field that excites the CSRR produces an intensified electric field around the CSRR region, providing a larger fringing electric field area. An inductive-capacitive (LC) tank circuit of a unit-cell CSRR can be defined by considering the duality theorem where each gap in the ring is represented by a shunt inductance and the CSRR-slot is represented by a capacitance [6]. The resonance frequency (f_r) of a single CSRR can be defined using the following equations:

$$C_{eff} = \frac{A\varepsilon_o\varepsilon_r}{s}, \tag{1}$$

$$f_r = \frac{1}{2\pi\sqrt{L_{eff}C_{eff}}}, \tag{2}$$

where $\varepsilon_{o,}\varepsilon_r$, A, s, L_{eff}, C_{eff}, and f_r represent the free-space permittivity, relative permittivity, area, split-gap of the CSRR, effective inductance, effective capacitance, and resonance frequency of the CSRR, respectively [7].

II. DESIGN OF THE CSRR-LOADED SENSOR ARRAY

A. SENSING MECHANISM OF THE PROPOSED CSRR-LOADED SENSOR ARRAY

The primary concept behind a typical RF crack sensor can be understood by considering that the presence of a crack in a metallic structure replaces that part of the metal with air, changing the effective permittivity (between the sensor and the metallic sheet); thus, the resonance frequency of the resonator shifts. In a conventional RF crack detection system, the sensors rely on a wider shift in the resonance frequency to distinguish a crack. However, instead of measuring the frequency shift, our proposed crack detection system relies on the difference in the transmitted magnitude. Fig. 1 illustrates the sensing mechanism of our proposed crack detection system. Because the proposed sensor consists of a 4 × 3 CSRR array, it can attain 12 pixels from the 4 channels and 3 CSRRs. The 4 channels are sequentially switched in a time domain by a single-pole four-throw (SP4T) switch. The changes in the power level at the three frequencies of the CSRRs are monitored in a frequency domain. The RF power detector converts the transmitted RF power level from the CSRR array into DC voltage, which is read by an analog-to-digital converter (ADC).

B. SENSOR DESIGN

The finite element method (FEM)-based ANSYS high-frequency structure simulator (HFSS) is used in this work. Starting from a single CSRR, a linear array of 1 × 3 CSRRs is designed in the ground plane of a microstrip line as illustrated in Fig. 2(a). The dielectric constant (ε_r) and tangential loss (tan δ) of a 0.6-mm-thick FR4 substrate are 4.4 and

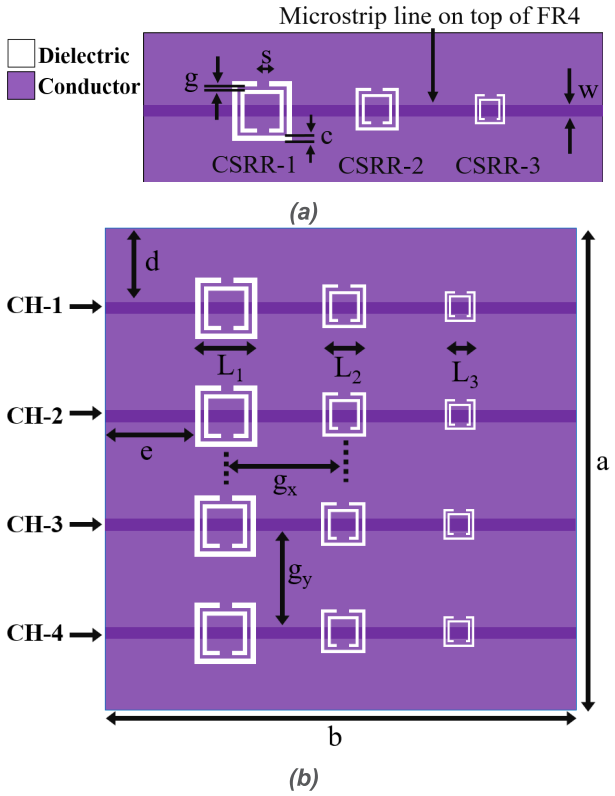

FIGURE 2. (a) Layout (back view) of a linear array of 1 × 3 CSRRs, (b) Layout (back view) of a 2-dimensional array of 4 × 3 CSRRs.

0.02, respectively. The geometrical parameters of the CSRR include split gap (s), coupling gap (g), and width (c) are chosen to be the same for all three CSRRs. Instead, three different side lengths (L_1, L_2, L_3) for CSRR-1, 2, and 3 are selected to generate three different resonance frequencies of 2.51 GHz, 3.45 GHz, and 4.39 GHz, respectively. The CSRRs are designed in the 1-4 GHz frequency range after considering availability of a commercial VCO in the desired frequency range. Mutual coupling between consecutive CSRRs is minimized to prevent the interference of the shifted resonance with the consecutive resonance [8].

To avoid mutual coupling between consecutive CSRRs, a minimum horizontal gap (g_x) and vertical gap (g_y) are chosen because larger g_x and g_y decrease the resolution of the proposed sensor. The 1 × 3 CSRR array is extended to the 4 × 3 CSRR array with four channels. Fig. 2(b) shows the final layout of the proposed 4 × 3 CSRRs. In addition, there is an insulating layer between the sensor array and aluminum sheet to isolate the conductive pattern of the proposed sensor and aluminum sheet with or without cracks. The submillimeter cracks are embedded in the surface of aluminum sheet, the thickness (h_{Al}) of which causes negligible changes, therefore, a 5-mm-thick aluminum sheet is chosen arbitrarily for this study [4]. The bulk conductivity of the 5-mm-thick aluminum sheet is set as $\sigma = 3.8 \times 10^7$ S/m in the ANSYS HFSS simulation. The polyethylene terephthalate (PET) film

TABLE 1. Design Parameters.

Parameter	*Dimension (mm)*	*Parameter*	*Dimension (mm)*
a	100	h_{Al}	5
b	100	L_1	6.7
c	0.4	L_2	5.3
d	11.925	L_3	4.4
e	20	s	0.5
g	0.2	w	1.15
g_x	30	W_c	1
g_y	23.85	L_c	10
h	0.6	D_c	0.1
h_{PET}	0.1		

with a thickness $h_{PET} = 0.1$ mm is used as the insulating layer. Its dielectric constant and tangential loss are set as 2.1 and 0.001, respectively. The final geometrical parameters are listed in Table 1.

Fig. 3(a) shows the simulated magnitude of the transmission coefficients of the 4 × 3 CSRR-loaded sensor array at CH-1, 2, 3, and 4 (S_{21}, S_{43}, S_{65}, and S_{87}, respectively). Each channel shows identical transmission coefficients. Fig. 3(b), (c), and (d) show the magnitude of the electric field at 2.51 GHz, 3.45 GHz, and 4.39 GHz, respectively. It is observed that the first resonance at 2.51 GHz is generated from CSRR-1. The second and third resonances at 3.45 GHz and 4.39 GHz are generated from CSRR-2 and 3, respectively.

C. SENSITIVITY TO CRACK SHAPES

We investigated the sensitivity of our proposed sensor array to detect various crack shapes such as long slots, zigzags, pinholes, and stars. Each shape is characterized by widths (W_c), crack lengths (L_c), and crack depths (D_c).

In each set, cracks of various shapes are simulated under CSRR-1, CSRR-2 and CSRR-3 and transmission magnitudes are shown in Fig. 4. From Fig. 4(a), we can see the transmission magnitude of each curve is detectable as compared to the reference power level (−9.42 dB) at 1.88 GHz and it is also noticeable that star shaped ($W_c = 0.1$ mm) and zigzag ($D_c = 0.2$ mm) cracks are distinguishable. The other two mentioned cases are marginally close to each other therefore our proposed crack sensor cannot distinguish cracks of all shapes though it can detect the cracks of various shapes.

We found that in addition to the shape of a crack, size/volume occupied by crack also influences the transmission magnitude. Cracks of three different shapes are simulated under CSRR-2 of CH-2 and transmission magnitudes are shown in Fig. 4(b). We can notice that long vertical slot ($W_c \times L_c \times D_c = 0.1$ mm × 5 mm × 0.1 mm) under CSRR-2 is not detectable because of considering a minimal slot

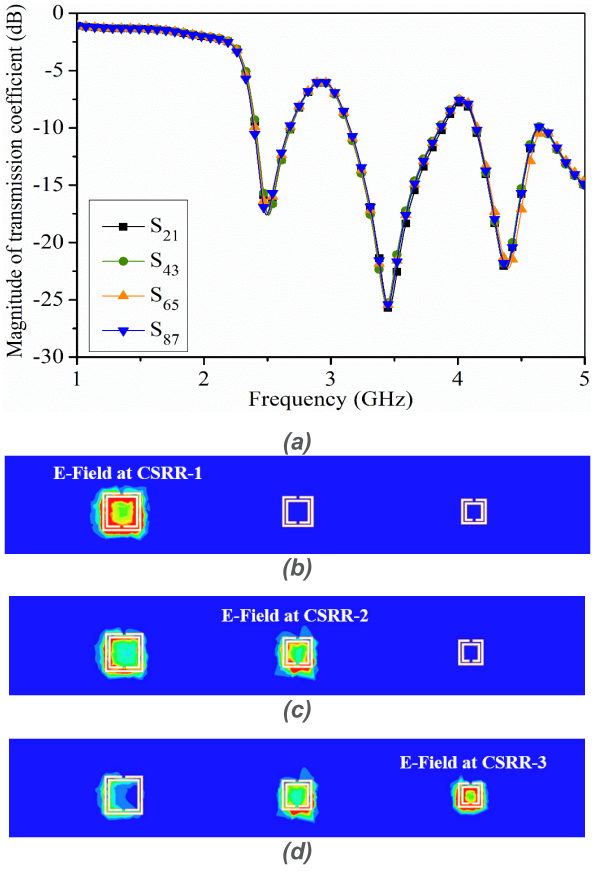

FIGURE 3. (a) Simulated transmission coefficient (magnitude) of the 4 × 3 CSRRs-loaded sensor array at CH-1, 2, 3, and 4. Simulated electric-field distributions at (b) 2.51 GHz, (c) 3.45 GHz, and (d) 4.39 GHz.

volume. Nevertheless, the star shape and the zigzag cracks under CSRR-2 are detectable as well as their shapes are distinguishable.

The cracks of four different shapes are simulated under CSRR-3 and the transmission magnitude of each curve is detectable as compared to the reference power level at 3.61 GHz, as shown in Fig. 4(c). Apparently, the shape of crack under CSRR-3 is not distinguishable using the resolution of current system design. We are of the opinion that crack detection depends upon orientation of crack, a certain minimal volume of crack, and perhaps shape of crack slot.

D. SENSITIVITY TO CRACK SIZES

The dimensions of the crack slot have its own characteristic along each xyz-axis thereby suggesting that identification of crack sizes cannot be relied only on volume variation. The parametric analysis of slot dimensions along each xyz-axis is performed and from them two peculiar cases are selected. Two crack slots under CSRR-3 having the same volume with different width and depth are analyzed and they exhibit an unequal magnitude of transmission coefficients at each volume distribution, as shown in Fig. 5(a).

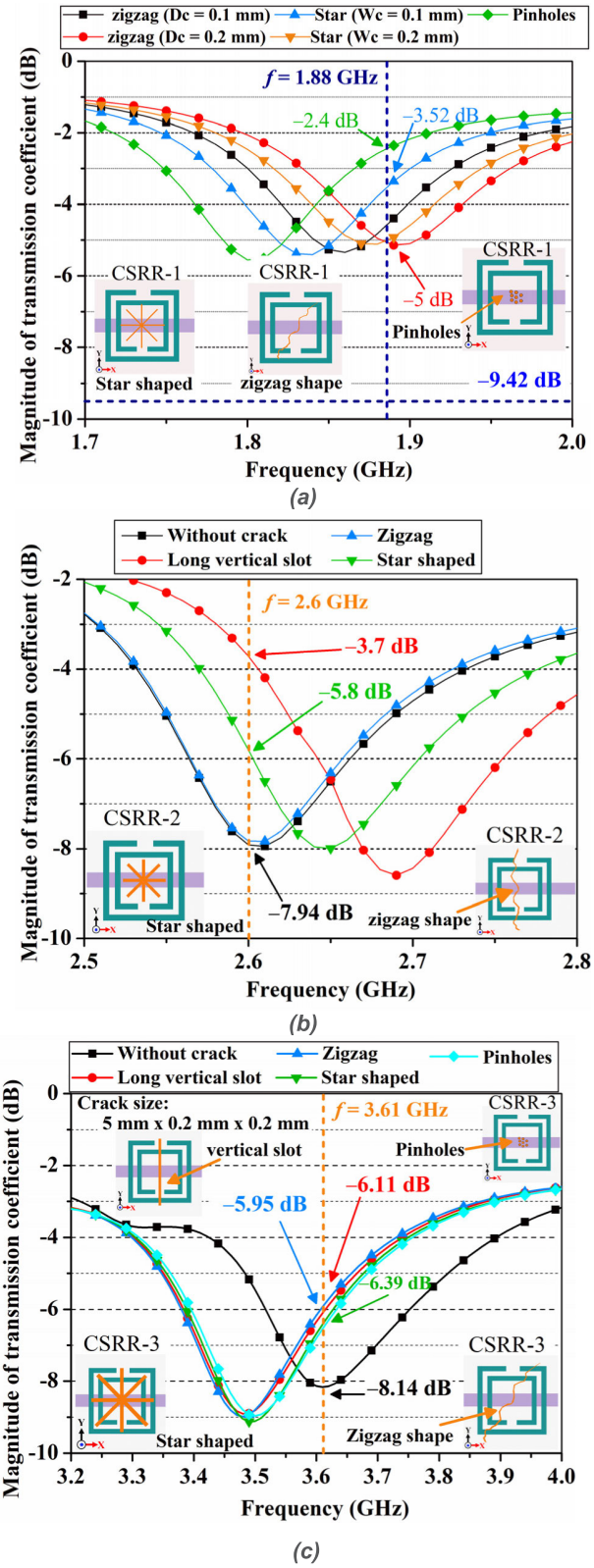

FIGURE 4. Magnitude of transmission coefficients obtained from simulating (a) star, pinholes, and zigzag shape cracks under CSRR-1 of CH-3. The depth of crack in each case is investigated for D_c = 0.1 mm and 0.2 mm. (b) vertical slot, star, and zigzag shape cracks under CSRR-2 of CH-2. (c) vertical slot, star, pinholes, and zigzag shape cracks under CSRR-3 of CH-3.

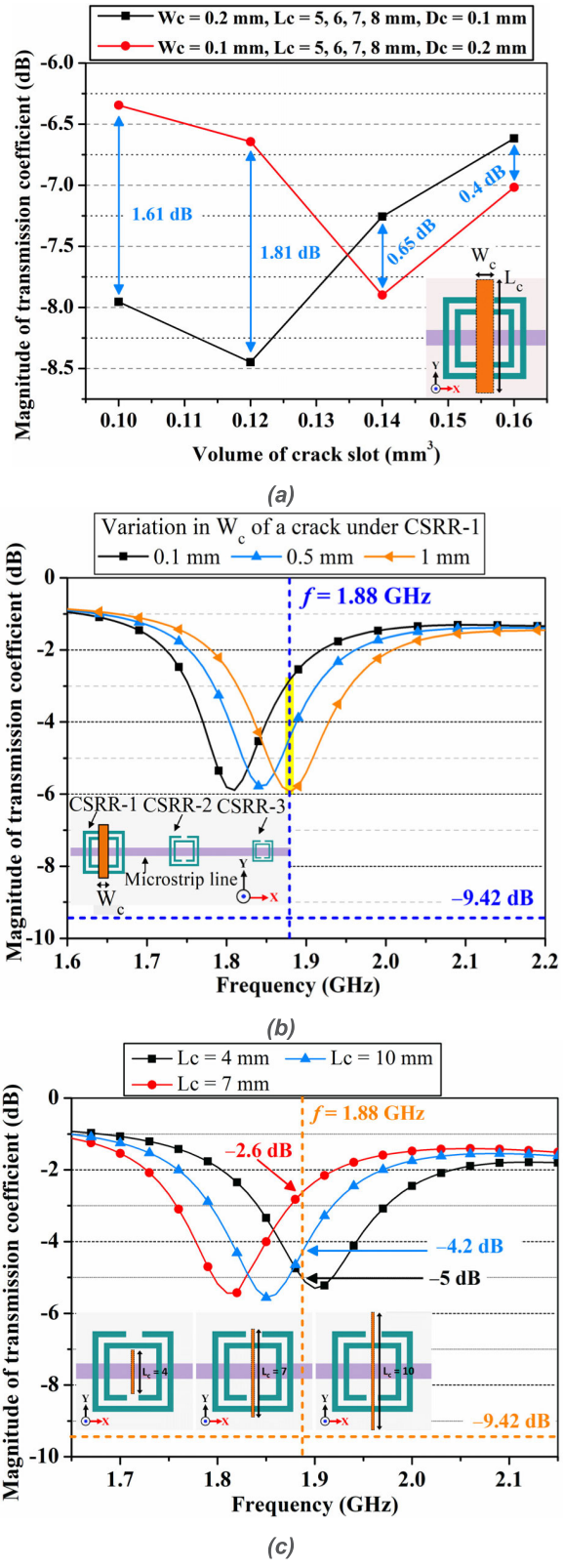

FIGURE 5. (a) Magnitude of transmission coefficients obtained from (a) two crack slots with equal volumes but different width and depth. (b) the variations in width (W_c) when the crack ($L_c \times D_c$ = 10 mm × 0.1 mm) was positioned under CSRR-1. (c) the variations in length (L_c) when the crack ($W_c \times D_c$ = 0.2 mm × 0.1 mm) was positioned under CSRR-1 of CH-3.

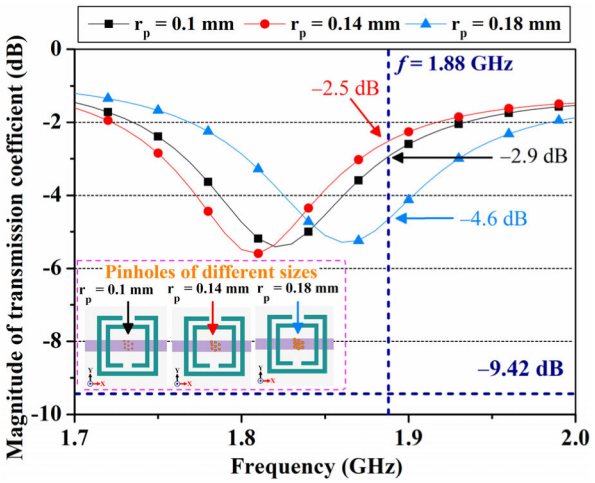

FIGURE 6. Magnitude of transmission coefficient obtained from variations in radii (r_p denotes radius of each hole) of pinholes when positioned under CSRR-1 of CH-3. The depth of pinholes is considered D_c = 0.1 mm in each case.

We conclude that crack size cannot be determined by monitoring only volume information because different combinations of width/length/depth of a crack slot can constitute the same volume.

In this section, we investigated the sensitivity of our proposed sensor array to detect various crack widths (W_c), crack lengths (L_c), crack depths (D_c), and pinholes radii (r_p). The localized electric field magnitude generated by CSRR-1 was unequal compared with the electric fields generated by CSRR-2 and CSRR-3 because of the different dimensions of each CSRR. An increase in crack width with the corresponding CSRR caused a decrease in capacitance and shifted the resonance frequency to a higher value, changing the transmission coefficient. A vertical crack under CSRR-1 is considered and the resulting magnitudes of the transmission coefficient with variations in W_c and L_c were analyzed as shown in Figs. 5 (b) and (c), respectively.

The slot cracks with W_c = 0.1 mm, 0.5 mm and 1 mm are detectable and distinguishable as can be seen in Fig. 5(b). Similarly, the slot cracks with L_c = 4 mm, 7 mm, and 10 mm are detectable and distinguishable as can be seen in Fig. 5(c). In these figures, the reference resonance frequency of CSRR-1 is 1.88 GHz and the reference power level is −9.42 dB.

To expand the sensitivity analysis, pinholes crack of various radii positioned under CSRR-1 were considered and the change in the magnitude of the transmission coefficients was analyzed in Fig. 6. We can see that the pinholes crack with all the three investigated radii (r_p = 0.1 mm, 0.14 mm, and 0.18 mm) are detectable as compared to the reference power level at 1.88 GHz, however, the size of former two radii are indistinguishable with respect to each other.

Next, a vertical crack ($W_c \times L_c \times D_c$ = 0.5 mm × 10 mm × 0.1 mm) under CSRR-2 and CSRR-3 was considered and, similar to CSRR-1, an increase in crack width

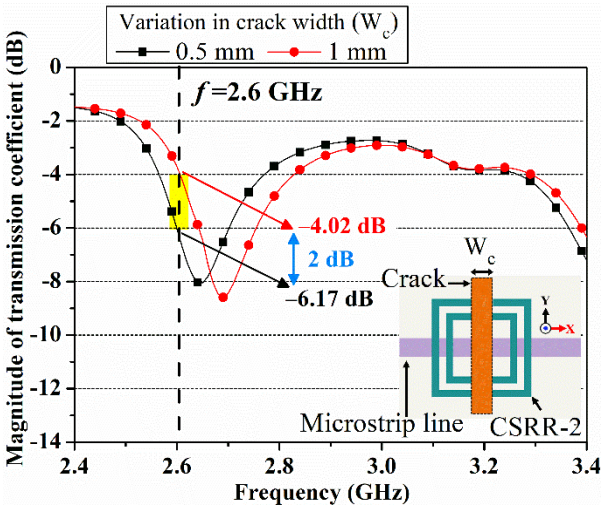

FIGURE 7. Analysis of the power levels to demonstrate the sensitivity of our proposed sensor to crack widths.

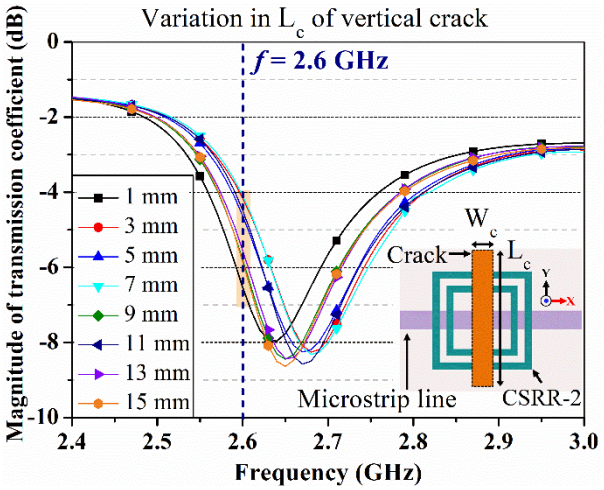

FIGURE 9. Magnitude of transmission coefficient obtained from variations in the crack length (L_c) where W_c = 1 mm and D_c = 0.1 mm.

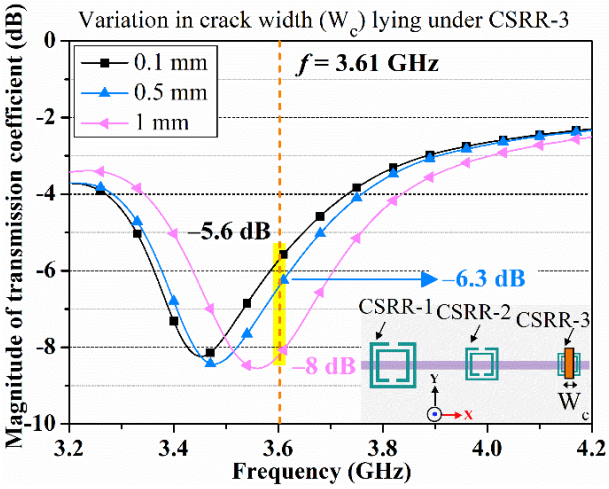

FIGURE 8. Magnitude of transmission coefficients obtained from the variations in width (W_c) when the crack (L_c × D_c = 10 mm × 0.1 mm) was positioned under CSRR-3.

caused a change in the transmission coefficient. To demonstrate that the proposed sensor is sensitive to submillimeter crack widths, Fig. 7 shows that the change of W_c from 0.5 mm to 1 mm caused a 2-dB change in the power level, which was detectable using our proposed crack detection system. Fig. 8 shows that the long slot crack under CSRR-3 with $W_c = 0.1$ mm and 0.5 mm are detectable, however, the power level produced from the crack with $W_c = 1$ mm is too close to the reference power level and thus cannot be detected. Nevertheless, our proposed CSRR-loaded array can reliably detect submillimeter cracks.

To demonstrate the sensitivity of our proposed crack sensor to crack lengths (L_c), a vertical crack ($W_c \times L_c \times D_c$ = 1 mm × 1 mm × 0.1 mm) was evaluated and the transmission coefficients for variations in L_c from 1 mm to 15 mm are plotted in Fig. 9. The difference in the power levels corresponding to 1 mm and 3 mm is detectable. Full-length longer cracks (the size of the substrate used) can also be easily detected using our proposed detection system because it utilizes the SP4T switch, enabling us to scan the CSRRs of each selected channel.

To demonstrate the sensitivity of our proposed crack sensor to crack depth (D_c), a zigzag crack is positioned under CSRR-1 of CH-3 and resulting transmission magnitudes are shown in Fig. 10. When D_c of the zigzag crack varied from 0.1 mm to 0.9 mm with a step size of 0.2 mm, all curves showed distinguished power levels except the one with 0.1 mm. We attribute this non-detectable lowest depth (0.1 mm) crack to the crack volume below the threshold because the width of the zigzag crack at some portions was less than 0.1 mm.

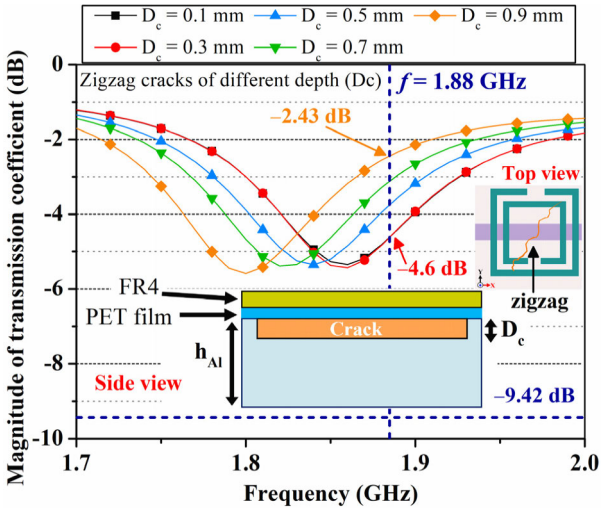

FIGURE 10. Analysis of the power levels to demonstrate the sensitivity of our proposed sensor to crack depth when a zigzag crack is considered under CSRR-1 of CH-3.

The depth (D_c) of a vertical crack positioned in the XY-plane (under CSRR-2) was varied from 0.1 mm to 0.9 mm with a step size of 0.3 mm and the change in the transmission coefficients is plotted in Fig. 11. Although the amplitude levels corresponding to 0.5 mm, 0.9 mm, and 0.1 mm are close to one another, the measurements can be reliably distinguished using a highly sensitive detector.

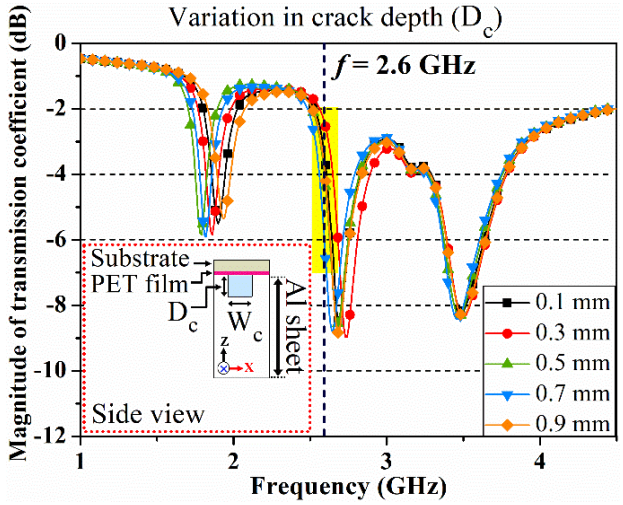

FIGURE 11. Analysis of the power levels to demonstrate the sensitivity of our proposed sensor to crack depth of a long slot crack under CSRR-2.

The same zigzag shaped crack of same variable width as already analyzed in Fig 4, now diagonally positioned under CSRR-2. For a variation in crack depth (D_c), the transmission magnitudes are shown in Fig. 12. The crack depth (D_c = 0.1 mm and 0.3 mm) causes transmission magnitudes whose relative difference from reference level is beyond the threshold value and thus they are not detectable with the given conditions. The crack with D_c = 0.5 mm produces a difference of transmission magnitude (2.14 dB) lying in the threshold region and thus this peculiar shaped zigzag crack can be detected using our proposed crack detection system.

To demonstrate the capability of our sensor to detect multiple cracks, three cracks of the same size ($W_c \times L_c \times D_c$ = 1 mm × 35 mm × 0.1 mm) under CSRR-1, CSRR-2, and CSRR-3 of CH- 2 were simulated and the transmission coefficients are plotted in Fig. 13. The changes in the power levels corresponding to both cases of W_c (1 mm and 2 mm) are distinguishable with respect to the reference power levels. Thus, multiple cracks of different sizes are detectable with our proposed sensor.

E. SENSITIVITY TO CRACK LOCATIONS AND ORIENTATIONS

The sensitive zone of each CSRR is evident from the E-field distribution plot and now we perform numerical simulations to identify the location of a crack. A vertical crack slot is moved with a step of 2-mm in horizontal direction.

Then, a crack slot oriented in horizontal direction is moved with a step of 2-mm in vertical direction. The transmission

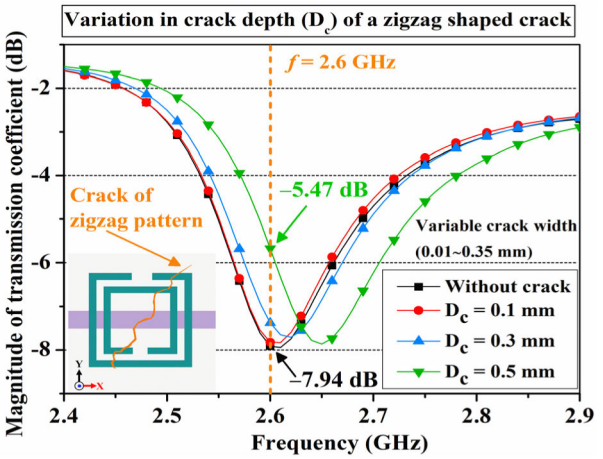

FIGURE 12. Simulated transmission coefficient magnitude of CH-2 when zigzag shaped cracks of various depths are considered under CSRR-2. The width of zigzag pattern varies from 0.01 mm (minimum) to 0.35 mm (maximum). Inset shows zigzag pattern crack diagonally positioned under CSRR-2. The crack depth (D_c) is considered along positive Z-axis.

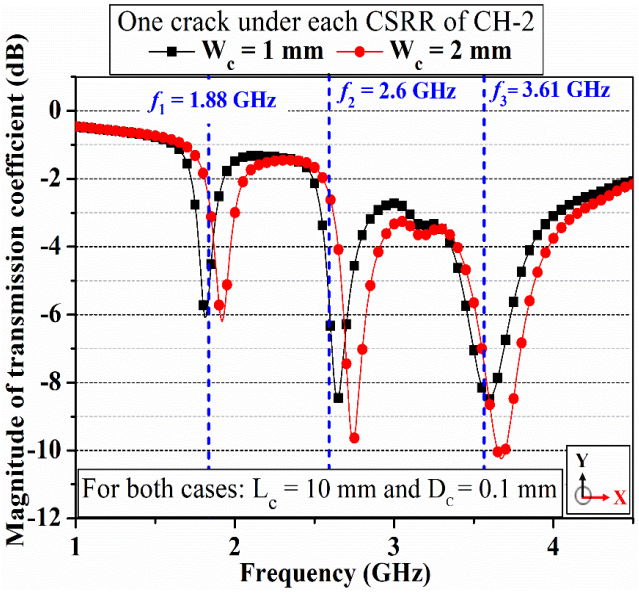

FIGURE 13. Transmission coefficients for three cracks of the same size ($W_c \times L_c \times D_c$ = 1 mm × 35 mm × 0.1 mm) under CSRR-1, CSRR-2, and CSRR-3 of CH-2 are simulated. For another case, W_c = 2 mm was simulated.

coefficients obtained from both of these scans are shown in Fig. 14. The CSRR-3 overlapped area is highlighted in both cases. We already mentioned in Fig. 3(c) that the E-field of each CSRR is confined to the size of individual CSRR, therefore scans overlapped with CSRR-area is of significant importance. The distinguished power levels obtained from a step of 2-mm scan in each horizontal/vertical direction indicate that cracks existing within a narrow region of CSRR-area can be located, as can be seen from Fig. 14 (a, and b). In order to avoid mutual coupling and minimize the electromagnetic interference, the existence of dead zones between consecutive CSRRs in horizontal/vertical direction is a realistic scenario

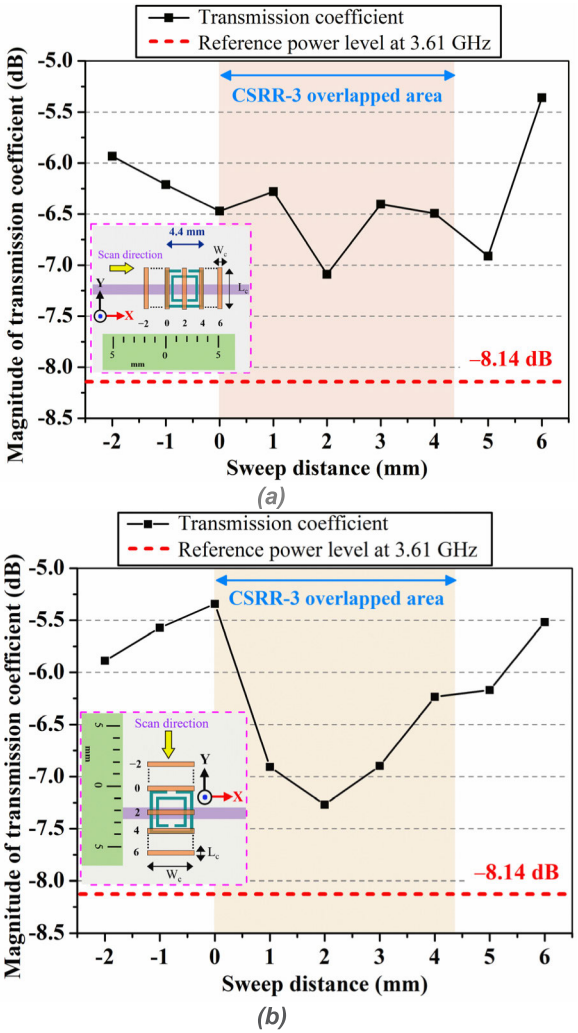

FIGURE 14. Analysis of the power levels to demonstrate the sensitivity of our proposed sensor to crack locations when (a) a vertical crack slot is horizontally moved under CSRR-3 of CH-3. (b) a horizontal crack slot is vertically moved under CSRR-3 of CH-3.

with current design. In future, an improved sensing technique can be envisaged. For instance, two layers sensing can be opted in which underlying layer could be designed to complement dead zones of the upper layer.

To demonstrate the sensitivity of our proposed crack detection sensor to various orientations, a crack slot horizontally oriented (labeled as 0°) was rotated 30° and then 60° and the resulting power levels are compared in Fig. 15. A horizontal crack under CSRR-2 with ($W_c \times L_c \times D_c = 10\,\text{mm} \times 1\,\text{mm} \times 0.1\,\text{mm}$) is detectable. The distinguished responses obtained for rotations of 0°, 30° and 60° demonstrate the possibility of crack growth speculation and, with a rigorous analysis, a diagnosis of crack growth can be determined.

F. SYSTEM INTEGRATION

A linear sensing array of 1 × 3 unit cells can detect up to three cracks. Contrary to a linear array, our proposed 4 × 3 CSRR-loaded array provides an increase in the scanning area

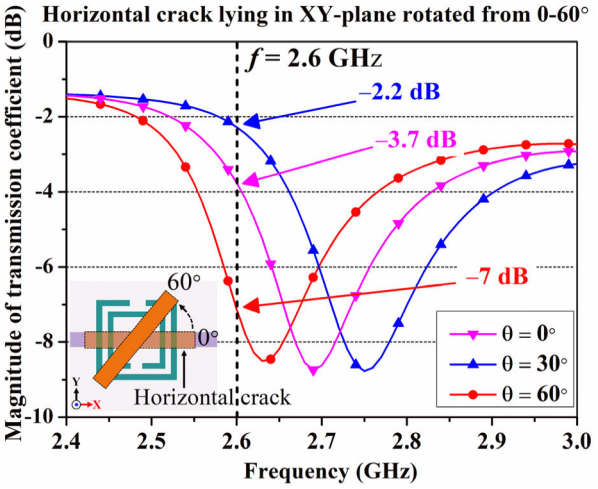

FIGURE 15. Demonstration of our proposed crack detection capability to detect crack orientations. The inset shows a horizontal crack and its rotated version at 60°. In each case, the dimensions of the crack are $W_c \times L_c \times D_c = 10\,\text{mm} \times 1\,\text{mm} \times 0.1\,\text{mm}$.

that is not a simple four-time enhancement of the sensitivity of a 1 × 3 linear array. The costs of the additional circuitry (connecting cables and RF switch for channel selection at the input and output of the sensor module) increased by a small amount, whereas the demonstrated advantages increased on a larger scale. Using a block diagram (Fig. 16(a)), we explain the functionality of each RF component involved in our proposed crack detection system. The VCO provides the required frequency to operate the CSRRs, and each SP4T switch is employed at the input/output side of the multiple crack detection system to select one channel at a time. The RF power detector converts input RF power into an RMS voltage, which is fed into an ADC (built-in on an Arduino UNO board). We used a VCO (DCYS200400-5) [9], RF power detector (ADL5920) [10], and SP4T switch (ADRF5040) [11]. The reference data (three resonance frequencies and corresponding power levels) are obtained from the crack free aluminum sheet, labeled as ''Precondition'' in the flow chart (Fig. 16(b)).

III. EXPERIMENTAL RESULTS

A. CHARACTERIZATION

Fig. 17(a) shows the fabricated prototype sensor board. To characterize the power levels of the proposed sensor with the aluminum sheet, the transmission coefficient magnitude was measured in each case (with/without crack) using a vector network analyzer (VNA), as shown in Fig. 17(b). Cracks of various sizes and orientations were embedded in the aluminum sheets and two examples of the fabricated specimen are shown in Fig. 17(c), and (d). Single/multiple cracks in multiple channels and orientations were required to demonstrate our proposed sensor's multiple crack detection capability as shown in Fig. 17(d). RF switches, low-loss connecting cables (coaxial), and the VCO board were not connected during this characterization.

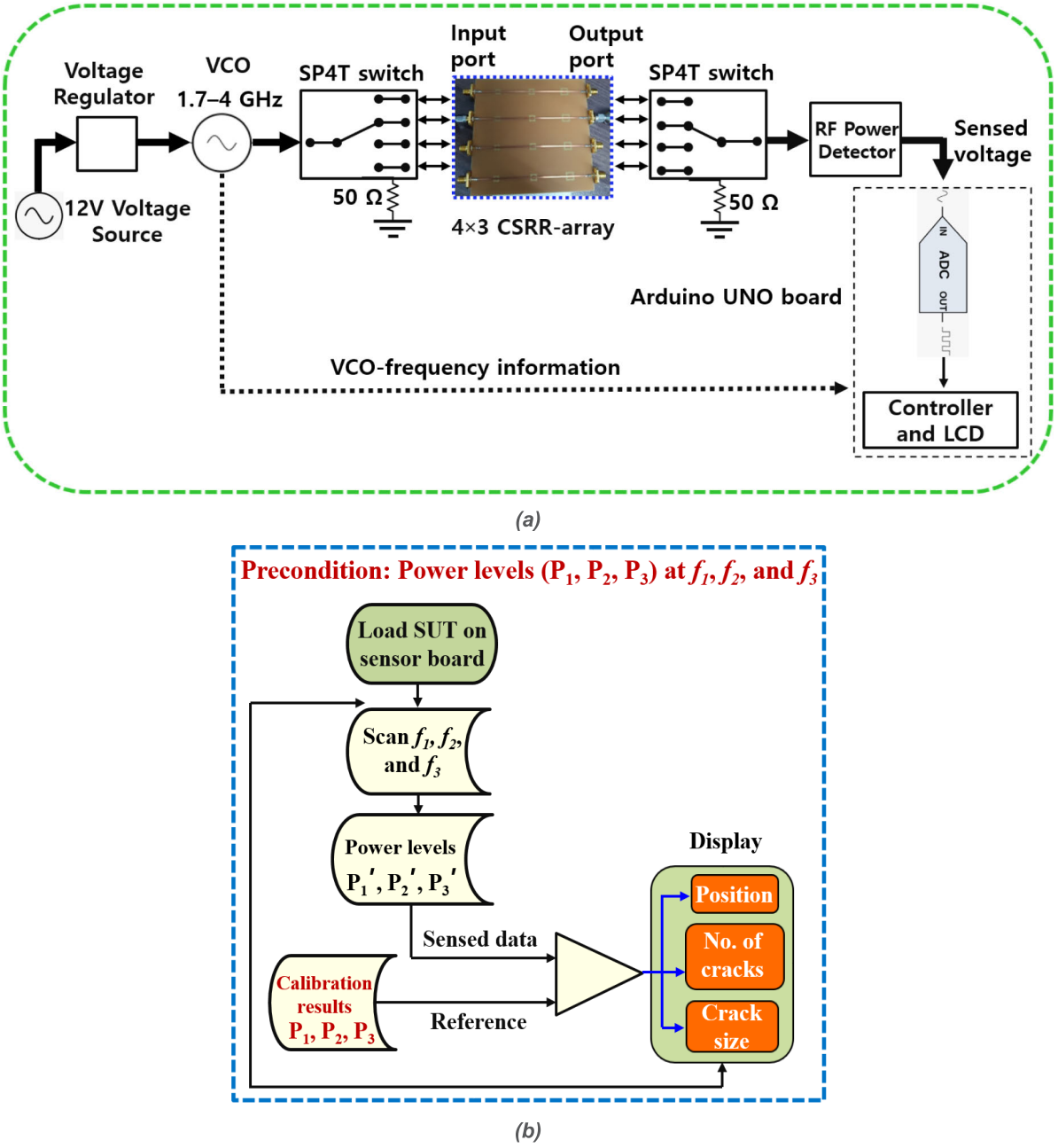

FIGURE 16. (a) Block diagram of the proposed crack detection system showing each RF component and sensor module, (b) the algorithm modeling behind our proposed system. Sample under test (SUT) is loaded on the sensor board and calibration data {power levels (P_1, P_2, and P_3) at reference frequencies (f_1, f_2 and f_3)} is compared with sensed data (P_1', P_2', and P_3'). Our proposed algorithm relies on the difference of power level obtained from Aluminum sheet without crack (calibration data) and Aluminum sheet having cracks (sensed data).

To calibrate the cable loss and loss of each switch, all the components were connected and voltages were measured using a digital multimeter (DMM) for the three desired frequencies (see Table 2). DC voltage levels obtained for three operating frequencies are distinguishable owing to different transmission magnitude and thus multiple cracks detected with high resolution are demonstrated.

B. MEASUREMENTS

The VCO board, SP4T switch, CSRR sensor array, and RF power detector were connected using 50-ohm RG316 low-loss coaxial cables. Fig. 18 shows the measurement setup. To determine the minimum power level that can be reliably detected using our proposed crack detection system, input RF power from the signal generator was varied where the

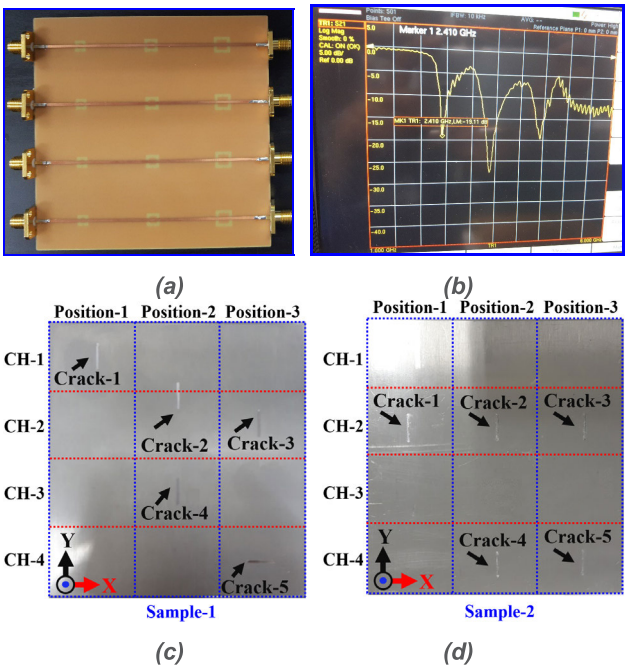

FIGURE 17. a) Fabricated prototype sensor developed on a low-cost FR4, (b) Transmission coefficient characterization of the fabricated prototype sensor array using a VNA. (Reference data), (c) Submillimeter cracks embedded in an aluminum sheet. The dimensions of cracks 1-3 are $W_c \times L_c \times D_c = 1$ mm $\times$ 10 mm $\times$ 0.2 mm, crack 4: $W_c \times L_c \times D_c = 1$ mm $\times$ 10 mm $\times$ 0.5 mm, and crack 5: $W_c \times L_c \times D_c = 10$ mm $\times$ 1 mm $\times$ 0.2 mm, (d) Specimen to demonstrate multiple crack detection capability; three cracks of the same size are embedded in CH-2 at the positions of CSRR-1, CSRR-2, and CSRR-3. The dimensions of all 5 cracks are $W_c \times L_c \times D_c =$ 1 mm $\times$ 10 mm $\times$ 0.1 mm. Aluminum sheet along x and y axis are considered as 90 mm $\times$ 100 mm, respectively.

TABLE 2. Amplitude levels at output of RF power detector for various cases.

VCO Frequency (GHz)	Without crack (Reference) (volts)	Multiple cracks (CH-2: Position-1, 2, 3) (volts)	Single crack (CH-2: Position-2) (volts)
1.804	1.427	1.749	1.738
2.609	1.298	1.503	1.470
3.61	0.3	1.044	0.770

output DC voltage received from the power detector is plotted in Fig. 19(a).

It can be observed that the built system is capable of detecting a signal as low as −40 dBm. The minimum read range of the RF power detector and the ADC's capability to resolve two consecutive voltage levels contribute to an overall high-resolution system. The resolution of the constructed system can be determined by inspecting the relationship between the voltages received at the output of the power detector and input signal applied. A commonly used 10-bit ADC with a 5-V input was used, producing a resolution that amounts to

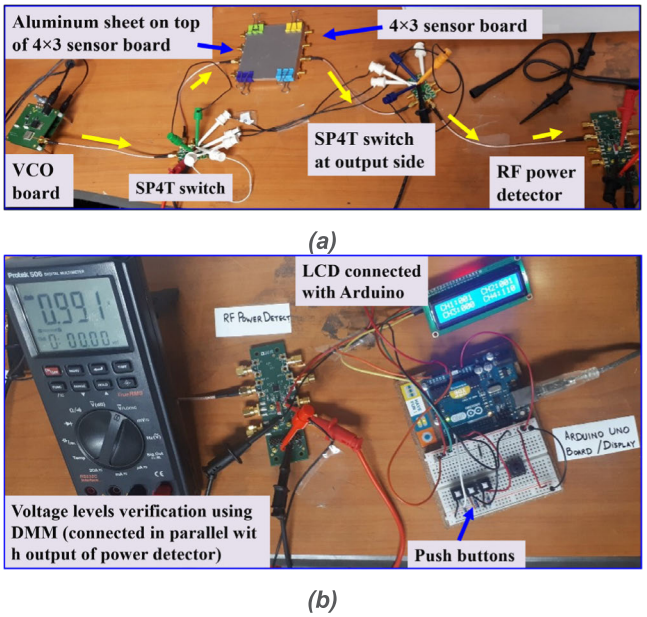

FIGURE 18. Complete system design to detect multiple cracks, sizes, and positions. (a) Fabricated sensor board and RF components are integrated and an aluminum specimen is tested, (b) Testing and characterization of voltage levels corresponding to various cases of crack detection.

4.88 mV. From Fig. 19(b), it can be observed that even a 1-dB voltage is detected at the output of the RF power detector; however, a minimum voltage of 2 dB is required to be detected at the ADC. Although positions-1/2/3 were defined on the tested specimen, a scanning range of the individual CSRRs in a channel was still required. A crack with fixed dimensions ($W_c \times L_c \times D_c = 1$ mm $\times$ 10 mm $\times$ 0.1 mm) was moved from the reference position (edge of CSRR-2) and the transmission coefficient magnitudes at the reference frequency are plotted against the scanned length in Fig. 19(c), from which it can be observed that the sensitive zone of a CSRR is closely confined to its boundary as expected from the E-field distribution (plotted at the resonance frequency) across a CSRR region (referring to Fig. 3(c)). The regions marked as A and C are beyond the detection zone with the current system design. Nevertheless, our proposed sensor system has demonstrated that it can perform 2-D scans because the resonances and power levels of the CSRRs for each selected channel are scanned.

A coding scheme can better explain the information displayed on the LCD shown in Fig. 18(b). Table 3 illustrates the coding scheme to indicate the number of cracks and their positions. The presence/absence of a crack is indicated by 1/0 and position-1/2/3 represents a specific portion corresponding to CSRR-1/CSRR-2/CSRR-3, respectively. Positions are defined in Fig. 17. For instance, for the embedded cracks shown in Fig. 17(c), the code displayed on the LCD is 100, 001, 010, and 001 for channels 1-4, respectively. Now consider the special case of crack-2. As shown in Fig. 17(c), crack-2 lies between two channels (CH-1 and CH-2) and the

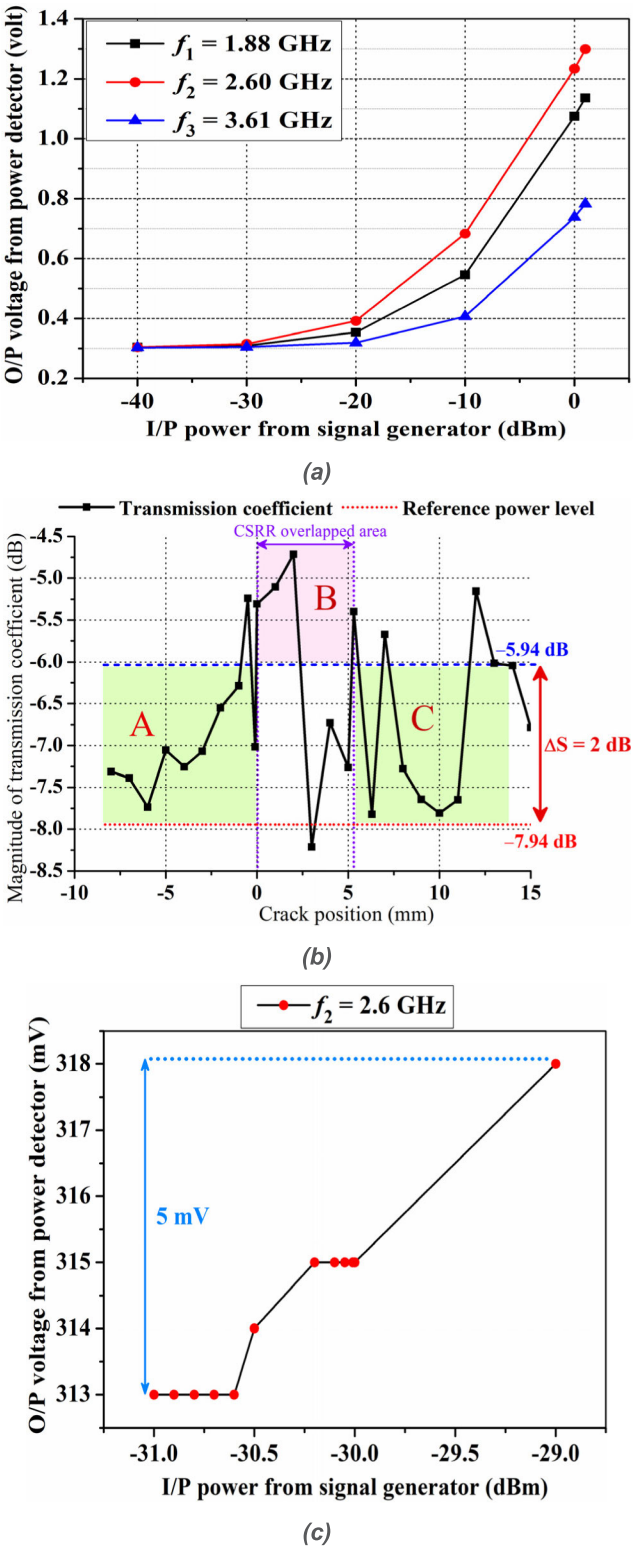

FIGURE 19. Characterization of the complete system to determine the minimum detectable power level and resolution of the system. (a) Output voltage received at the power detector with variations in the applied input power, (b) Resolution characterization of the system by investigating the input power applied and the output voltage received at the power detector whereas ΔS = 2dB denotes difference in power levels, (c) Sweep of the crack position under CSRR-2. A crack with dimensions $W_c \times L_c \times D_c$ = 1 mm × 10 mm × 0.1 mm is considered for this analysis.

TABLE 3. Coding illustrations of the crack position using the proposed 4 × 3 sensor array.

Channels 0: No crack, 1: Crack	Position-1	Position-2	Position-3
Channel-1/2/3/4	0	0	0
	1	0	0
	0	1	0
	0	0	1
	1	1	0
	1	0	1
	0	1	1
	1	1	1

crack length is 10 mm, which is beyond the sensitive zone of the individual CSRR, and thus cannot be detectable.

IV. PERFORMANCE EVALUATION

A. COMPARISON WITH CONVENTIONAL RF TECHNIQUES

We selected the most recently published articles for comparison (Table 4); however, only two of these crack sensors are capable of detecting submillimeter cracks.

In [1], a microstrip patch with a rectangular shape generates two resonance frequencies (f_{01} and f_{10}) that produce different responses only when a crack exists at the diagonal of the rectangular patch. In [3], a 3 × 3 cross-shaped passive FSS is an array structure. In [12], the crack length was varied from 0 mm to 14 mm for two typical cases (30° and 60° rotations) and a prominent change in the measured resonance frequency was observed for cracks longer than 4 mm. The satisfactory performances of expensive RFID tags have been realized with the addition of external sensors [13].

B. COMPARISON WITH CONVENTIONAL NON-RF TECHNIQUES

To establish a comprehensive analysis, we present a crack detection system based on non-RF technology. For instance, a convolutional neural network algorithm based on information extracted from a video frame is proposed in [14]. They analyzed the detection of a 0.11-mm to 0.4-mm-wide crack on nuclear power plant surfaces. In [15], a 0.7-mm-wide fatigue-induced crack in a concrete slab is investigated using a laser displacement sensor. However, commercial software such as LabView installed on a computer is required to process and analyze the data.

C. COMPARISON WITH COMMERCIAL CRACK DETECTION SYSTEMS

A commercial crack detection sensor based on optical fiber technology was developed by [16]. They claim minimum

TABLE 4. RF Crack sensors: Multiple crack detection capability and size of minimum detectable crack.

Ref. #	Technology	Operating frequency [GHz]	Frequency shift [MHz]	Substrate/ material	System Design	Minimum detectable crack [mm] ($W_c \times L_c \times D_c$)*	No. of detectable cracks
[4]	CSRR-SIW	5	600	Rogers LM6010	No	1×35×1	1
[18]	CSRR	5	240	Rogers RO4350	No	$W_c = 0.1$	1
[3]	3×3 cross shaped FSS†	10.16	640	Polyimide film	No	$L_c = 72$	1
[1]	Patch	2–2.4	90	Alumina ceramic	No	0.2×50×2	2
[12]	Patch	1.8, 2.5	N/A	FR4	No	$L_c = 2$	1
[19]	Chipless RFID	3.29–4.7	13.43 MHz/mm	Taconic CER-10-0500	No	$W_c \times L_c = 1 \times 15$	1
[20]	RFID	0.850–0.950	N/A	N/A	Yes	$W_c = 1$	1
This work	CSRR array	1.5–3.5	N/A	FR4	Yes	1 ×10×0.1	12

*($W_c \times L_c \times D_c$) represents crack width, crack length, and crack depth in mm.
†Frequency selective surface (FSS)
**Ethyl-vinyl acetate (EVA)
All are proposed to detect cracks on metallic surfaces, except [20], which detect cracks on non-metallic surfaces.

detectable crack widths of 0.05 mm, 0.1 mm, 0.2 mm, and 0.3 mm. Another commercial crack detection system developed by [17] is a position-sensitive device. The specifications for this system are: operating speed = 50.8 mm/second and resolution = 0.0762 mm [17]. Because the sensor mechanically slides, it provides slower measurements than an RF crack detection system. Moreover, these types of displacement sensors require data logging (signal processing) devices to interpret the measured data, the size of which eventually becomes large. Existing commercial products exhibit superior performance but at the expense of high costs and increased complexity. Not only is our proposed CSRR-loaded sensor array for crack detection applications a low-cost solution, but it can also detect submillimeter cracks. Additionally, the resolution can be further enhanced. For instance, using a 12-bit ADC, our constructed system can resolve two spatially closed cracks with a difference of a 0.5-dB voltage for the same reference.

V. CONCLUSION

We present our proposed crack detection sensor, in the first place to detect single/multiple cracks and secondly, to detect cracks of various shapes, and sizes, and lastly, it can be used to locate the position of cracks. Our proposed 4 × 3 CSRR-loaded array is developed on a low-cost FR4 substrate. After constructing the complete system, we change the tuning voltage of the VCO to adjust the frequency of each CSRR. The sensed signal is fed to an RF power detector that converts the signal into voltages that are read by an ADC. The differences in voltage levels induced by a crack are compared in a microcontroller using an Arduino board. Submillimeter cracks of various sizes and orientations are experimentally demonstrated. In fact, our crack detection system successfully demonstrates the detection of a minimum detectable crack with dimensions $W_c \times L_c \times D_c = 1\,\text{mm} \times 10\,\text{mm} \times 0.1\,\text{mm}$. By adopting a system design approach, we eliminate the need for a VNA, which is a bulky and expensive device. More importantly, relying on voltage levels for crack detection greatly enhances the crack detection sensitivity.

REFERENCES

[1] H. Dong, W. Kang, L. Liu, K. Wei, J. Xiong, and Q. Tan, "Wireless passive sensor based on microstrip antenna for metal crack detection and characterization," *Meas. Sci. Technol.*, vol. 30, no. 4, Feb. 2019, Art. no. 045103.
[2] I. Mohammad, V. Gowda, H. Zhai, and H. Huang, "Detecting crack orientation using patch antenna sensors," *Meas. Sci. Technol.*, vol. 23, no. 1, Jan. 2012, Art. no. 015102.
[3] S.-D. Jang, B.-W. Kang, and J. Kim, "Frequency selective surface based passive wireless sensor for structural health monitoring," *Smart Mater. Struct.*, vol. 22, no. 2, Feb. 2013, Art. no. 025002.
[4] T. Yun and S. Lim, "High-Q and miniaturized complementary split ring resonator-loaded substrate integrated waveguide microwave sensor for crack detection in metallic materials," *Sens. Actuators A, Phys.*, vol. 214, pp. 25–30, Aug. 2014.
[5] A. Albishi and O. Ramahi, "Detection of surface and subsurface cracks in metallic and non-metallic materials using a complementary split-ring resonator," *Sensors*, vol. 14, no. 10, pp. 19354–19370, Oct. 2014.
[6] J. D. Baena, J. Bonache, F. Martin, R. M. Sillero, F. Falcone, T. Lopetegi, M. A. G. Laso, J. Garcia-Garcia, I. Gil, M. F. Portillo, and M. Sorolla, "Equivalent-circuit models for split-ring resonators and complementary split-ring resonators coupled to planar transmission lines," *IEEE Trans. Microw. Theory Techn.*, vol. 53, no. 4, pp. 1451–1461, Apr. 2005.
[7] R. Marques, F. Martn, and M. Sorolla, *Metamaterials with Negative Parameters: Theory, Design, and Microwave Applications*. Hoboken, NJ, USA: Wiley, 2008.
[8] M. A. H. Ansari, A. K. Jha, Z. Akhter, and M. J. Akhtar, "Multi-band RF planar sensor using complementary split ring resonator for testing of dielectric materials," *IEEE Sensors J.*, vol. 18, no. 16, pp. 6596–6606, Aug. 2018.
[9] *Data Sheet VCO: Voltage Controlled Oscillator Surface Mount Model: DCYS300600-5*. Accessed: Oct. 25, 2019. [Online]. Available: http://www.synergymwave.com
[10] *Data Sheet Power Detector: Bidirectional RMS and VSWR Detector, ADL5920, 9 kHz to 7 GHz*. [Online]. Available: http://www.analog.com
[11] *Data Sheet ADRF5040: SP4T Nonreflective Switch, 9 kHz to 12 GHz*. Accessed: Oct. 25, 2019. [Online]. Available: http://www.analog.com
[12] L. Ke, Z. Liu, and H. Yu, "Characterization of a patch antenna sensor's resonant frequency response in identifying the notch-shaped cracks on metal structure," *Sensors*, vol. 19, no. 1, p. 110, 2019.
[13] M. Donelli, "An RFID-based sensor for masonry crack monitoring," *Sensors*, vol. 18, no. 12, p. 4485, Dec. 2018.

[14] F.-C. Chen and M. R. Jahanshahi, "NB-CNN: Deep learning-based crack detection using convolutional neural network and Naïve bayes data fusion," *IEEE Trans. Ind. Electron.*, vol. 65, no. 5, pp. 4392–4400, May 2018.
[15] P. Giri and S. Kharkovsky, "Detection of surface crack in concrete using measurement technique with laser displacement sensor," *IEEE Trans. Instrum. Meas.*, vol. 65, no. 8, pp. 1951–1953, Aug. 2016.
[16] *Tokyo Measuring Instruments Lab., Commercial Crack Detection Sensor for Concrete*. Accessed: Apr. 15, 2020. [Online]. Available: https://tml.jp/e/knowledge/special_ins/crack_detection.html
[17] *Micron Optics, Cleveland Electric Laboratories LCM-350 series Crack Sensor*. Accessed: Apr. 15, 2020. [Online]. Available: https://www.micronoptics.com/product/linear-position-sensors-copy/
[18] A. M. Albishi, M. S. Boybay, and O. M. Ramahi, "Complementary split-ring resonator for crack detection in metallic surfaces," *IEEE Microw. Wireless Compon. Lett.*, vol. 22, no. 6, pp. 330–332, Jun. 2012.
[19] A. M. J. Marindra and G. Y. Tian, "Chipless RFID sensor tag for metal crack detection and characterization," *IEEE Trans. Microw. Theory Techn.*, vol. 66, no. 5, pp. 2452–2462, May 2018.
[20] S. Caizzone and E. DiGiampaolo, "Wireless passive RFID crack width sensor for structural health monitoring," *IEEE Sensors J.*, vol. 15, no. 12, pp. 6767–6774, Dec. 2015.

AHMED SALIM (Student Member, IEEE) received the B.S. degree in electrical engineering from the University of Engineering and Technology, Lahore, Pakistan, in 2007, and the M.S. degree in electrical engineering from Linkoping University, Sweden, in 2011. He is currently pursuing the Ph.D. degree with the School of Electrical and Electronics Engineering, Chung-Ang University, Seoul, South Korea. His research interest includes designing microwave resonators for sensing applications.

AQEEL HUSSAIN NAQVI (Student Member, IEEE) received the B.S. degree in electrical engineering from the COMSATS Institute of Information Technology (CIIT), Islamabad, Pakistan, in 2011, and the M.S. degree in electrical engineering from the School of Electrical Engineering and Computer Sciences, National University of Sciences and Technology (NUST), Islamabad, in 2015. He is currently pursuing the Ph.D. degree with the School of Electrical and Electronics Engineering, Chung-Ang University, Seoul, South Korea.

His research interests include the design and the analysis of microwave and millimeter-wave antennas, reconfigurable antennas, programmable metasurfaced antennas, and planar and 3D printed antennas. He has served as a Technical Reviewer of the IEEE Antennas and Wireless Propagation Letters (AWPL). Also, he is a technical Review Editor on the Editorial Board of *System and Test-Bed Design* (specialty section of Frontiers in Communications and Networks).

ANH DUC PHAM (Student Member, IEEE) was born in Stollberg, Germany, in 1994. He received the B.Eng. degree in electrical engineering from the Hanoi University of Science and Technology, Hanoi, Vietnam, in 2017. He is currently pursuing the M.S. degree with the School of Electrical and Electronics Engineering, Chung-Ang University, Seoul, South Korea.

From 2017 to 2018, he was a RF Engineer with the Viettel Aerospace Institute, involved in researching and developing microwave circuits and systems. His research interests include millimeter-wave antennas, reconfigurable antennas, and metasurfaced antennas.

SUNGJOON LIM (Member, IEEE) received the B.S. degree in electronic engineering from Yonsei University, Seoul, South Korea, in 2002, and the M.S. and Ph.D. degrees in electrical engineering from the University of California at Los Angeles (UCLA), Los Angeles, CA, USA, in 2004 and 2006, respectively.

After a postdoctoral position at the Integrated Nanosystem Research Facility (INRF), University of California at Irvine, Irvine, CA, USA, he joined the School of Electrical and Electronics Engineering, Chung-Ang University, Seoul, Korea, in 2007, where he is currently a Professor. He has authored and coauthored more than 250 international conference, letter, and journal articles. His research interests include engineered electromagnetic structures (metamaterials, electromagnetic bandgap materials, and frequency selective surfaces), printed antennas, substrate integrated waveguide (SIW) components, inkjet-printed electronics, and RF MEMS applications. He is also interested in the modeling and design of microwave circuits and systems.

Prof. Lim received the Institution of Engineering and Technology (IET) Premium Award, in 2009, the ETRI journal Best Paper Award, in 2014, the Best Paper Award in the 2015 International Workshop on Antenna Technology (iWAT), the Best Paper Award in the 2018 International Symposium on Antennas and Propagation (ISAP), and the CAU Distinguished Scholar, from 2014 to 2020.